SOFT ROBOTS

# Soft robotic platform for progressive and reversible aortic constriction in a small-animal model

**Luca Rosalia[1,2]†, Sophie X. Wang[2,3]†, Caglar Ozturk[2], Wei Huang[4], Jean Bonnemain[2,5], Rachel Beatty[6], Garry P. Duffy[6], Christopher T. Nguyen[7], Ellen T. Roche[2,8]***



**Our understanding of cardiac remodeling processes due to left ventricular pressure overload derives largely from animal models of aortic banding. However, these studies fail to enable control over both disease progression and reversal, hindering their clinical relevance. Here, we describe a method for progressive and reversible aortic banding based on an implantable expandable actuator that can be finely tuned to modulate aortic banding and debanding in a rat model. Through catheterization, imaging, and histologic studies, we demonstrate that our platform can recapitulate the hemodynamic and structural changes associated with pressure overload in a controllable manner. We leveraged soft robotics to enable noninvasive aortic debanding, demonstrating that these changes can be partly reversed because of cessation of the biomechanical stimulus. By recapitulating longitudinal disease progression and reversibility, this animal model could elucidate fundamental mechanisms of cardiac remodeling and optimize timing of intervention for pressure overload.**

## INTRODUCTION

Left ventricular (LV) pressure (LVP) overload plays a key role in the onset of heart failure with preserved ejection fraction (HFpEF), which accounts for ~50% of all cases of heart failure (*1*, *2*). This biomechanical state is typically induced by conditions that cause an increase in the afterload, such as aortic stenosis (AS) and hypertension (*3*, *4*). HFpEF often arises as a result of remodeling processes caused by LV pressure overload, which induce stiffening of the LV wall and lead to the inability of the heart to fill adequately and therefore eject enough blood to meet the metabolic demands of the body (*5*, *6*). Treatments for HFpEF are now limited, with scarce medical therapy options and no HFpEF-specific US Food and Drug Administration–approved devices (*7*). The lack of therapeutics for these patients is largely due to our incomplete understanding of fundamental processes driving cardiac remodeling in HFpEF and the potential reversibility of these processes (*8*).

Aortic banding is a surgical technique involving partial ligation of the aorta that is broadly used to study cardiac remodeling processes due to pressure overload associated with HFpEF in preclinical models (*9*, *10*). There are many studies in the literature on aortic banding across various animal species that report nuances in the surgical approach and techniques for structural and functional evaluation. Consistently, these methods failed to enable control over the severity of aortic constriction and, simultaneously, over the dynamics of disease progression and reversal, hindering fundamental and translational studies of human disease. In small animals, aortic banding is performed at either the thoracic or the abdominal level. In turn, thoracic aortic banding can be done either at the ascending aorta or at the aortic arch, whereas abdominal banding involves aortic constriction above the origin of both renal arteries (*11*–*13*). Although it is the most challenging to perform from a surgical standpoint, ascending aortic constriction is the most relevant model of pressure overload due to AS (*14*, *15*). This is because, unlike other approaches, it does not induce pressure overload in the brachiocephalic artery or in the entire upper body circulation and is therefore more representative of the hemodynamics of AS compared with other techniques.

Different degrees of aortic banding can result in various levels of cardiac remodeling and diastolic dysfunction (*16*, *17*). The degree of constriction can be coarsely controlled by choice of the size of the needle used during ligation, which determines how tight the knot around the aorta will be (*18*). An alternative approach involves implantation of O-rings or clips with varying inner diameter dimensions (*19*–*21*). Neither of these techniques, however, enables temporal control over the degree of aortic banding, and, therefore, they fail to recreate pathophysiological processes of disease onset and progression that are clinically relevant. For example, implantation of a loose ring (or use of a large needle) results in a relatively mild degree of pressure overload, which fails to follow the natural progression observed over time in humans due to disease exacerbation. Contrarily, implantation of a tight ring (or small needle) causes an abrupt onset of severe pressure overload, which is rarely observed in patients. Another method, known as intermittent banding, involves tunneling of the suture to the back of the animal so that it can be tightened to induce intermittent pressure overload (*22*). Although this technique could capture cardiac remodeling processes triggered by intermittent stimuli, such as during exercise, it does not provide notable insights into pathophysiological processes associated with disease.

A major limitation of current small-animal models of aortic banding is their inability to reverse pressure overload. Reversal is crucial for studies of ventricular remodeling plasticity, which would advance our fundamental understanding of disease progression and enable direct study of the effects of therapeutics (*23*, *24*). Unfortunately, current approaches require surgical removal of the suture or

[1]Health Sciences and Technology Program, Harvard University - Massachusetts Institute of Technology, Cambridge, MA 02139, USA. [2]Institute for Medical Engineering and Science, Massachusetts Institute of Technology, Cambridge, MA 02139, USA. [3]Department of Surgery, Beth Israel Deaconess Medical Center, Boston, MA 02215, USA. [4]Koch Institute For Integrative Cancer Research, Massachusetts Institute of Technology, Cambridge, MA 02142, USA. [5]Department of Adult Intensive Care Medicine, Lausanne University Hospital, Lausanne 1011, Switzerland. [6]Anatomy and Regenerative Medicine Institute, College of Medicine Nursing and Health Sciences, University of Galway, Galway H91 W2TY, Ireland. [7]Department of Cardiovascular Medicine, Radiology, and Biomedical Engineering, Cleveland Clinic, Cleveland, OH 44195, USA. [8]Department of Mechanical Engineering, Massachusetts Institute of Technology, Cambridge, MA 02139, USA.
*Corresponding author. Email: etr@mit.edu
†These authors contributed equally to this work.

clip through an additional intervention, increasing animal morbidity and mortality rates (25 to 75%) associated with these studies (*19*, *20*, *25*–*27*). Together, limitations in these techniques highlight the need for an approach that enables controllability of the degree of aortic banding and modulation of the dynamics of disease progression and that provides a less invasive means to reverse pressure overload.

In previous work, we demonstrated the ability of soft robotic tools to recapitulate the hemodynamics of AS and HFpEF in a benchtop and a subacute swine model (*28*–*30*). Here, we describe the use of soft robotics for the development of a highly controllable chronic small-animal model of aortic banding that overcomes the shortcomings of other techniques. We leveraged invasive hemodynamic monitoring to evaluate clinical metrics of cardiac function and AS in the acute setting. Uniquely, we used magnetic resonance imaging (MRI) to visualize aortic flow resulting from aortic banding and to characterize the degree of aortic constriction, cardiac remodeling, and reversal in a chronic study.

## RESULTS

### Soft robotic actuator enabled controlled banding and debanding in a rat model

We designed and manufactured a soft robotic actuator composed of a relatively noncompliant [inner diameter (ID) = 0.8 mm, outer diameter (OD) = 2.4 mm, Durometer 70A, PVC, McMaster-Carr] and a compliant (ID = 0.8 mm, OD = 1.6 mm, Durometer 35A, silicone rubber, McMaster-Carr) tubing and a fabric sheet (0.2-mm-thick 70 Denier heat-sealable coated nylon taffeta, Seattle Fabrics) (Fig. 1A). Under pressure, the compliant tube (length, $l \approx 2$ mm) expanded from a deflated to an actuated state (Fig. 1A). The noncompliant tube ($l \approx 25$ mm) prevented expansion of the actuator beyond the compliant material, and the fabric sheet ($l \approx 2$ mm) allowed expansion in one direction only, away from the fabric. The compliant tubing was connected to the noncompliant tube through a carbon fiber tube (ID = 0.5 mm, OD = 1.0 mm, $l \approx 1.5$ mm) wrapped in a heat-shrink tube that reinforced the connection between the two tubings. A silicone rubber adhesive sealed the other end of the compliant material. The uniaxial tensile response of these materials (Fig. 1B) highlighted differences in their average ultimate tensile strength ($UTS_1 = 126.1$ MPa; $UTS_2 = 95.1$ MPa; $UTS_3 = 122.4$ MPa) and average maximum elongation ($\epsilon_1^{max} = 2.31$; $\epsilon_1^{max} = 2.77$; $\epsilon_1^{max} = 0.59$). Further, the fabric sheet was shown to exhibit elastic properties, whereas the tubes displayed a hyperelastic behavior. The average Ogden model coefficients were calculated to be $a_1 = 0.3583$ and $b_1 = 2.6303$ [coefficient of determination ($R^2$) = 0.9843] for the noncompliant tube and $a_1 = 0.0002$ and $b_1 = 4.7137$ ($R^2 = 0.9938$) for the more compliant tube (see Materials and Methods).

We quantified the radial expansion of the compliant tube for three different actuation levels (L1 to L3), achieved by injecting distinct volumes of glycerin as the actuation medium, namely, L1 = 0.26 ml, L2 = 0.28 ml, and L3 = 0.3 ml. These volumes were used to recreate (and progress between) distinct severities of pressure overload in in vivo experiments. Changes in the maximum radius of the expanding actuator, approximating the shape of a hemisphere, for the three levels are reported in Fig. 1C ($\Delta R_{L1} = 0.88$ mm; $\Delta R_{L2} = 1.29$ mm; $\Delta R_{L3} = 1.94$ mm). No remarkable expansion of the actuator was seen for actuation volumes less than ~0.24 ml. Figure 1D shows the corresponding maximum pressure measured inside the actuator at the three levels of actuation ($P_{L1} = 13.8$ psi; $P_{L2} = 16.1$ psi; $P_{L3} = 19.6$ psi). The pressure-volume characteristics of the actuator during continuous banding and debanding at constant-rate (0.1 to 0.2 ml/s) infusion and withdrawal of up to 3 ml of medium ($n = 5$) are shown in Fig. 1E.

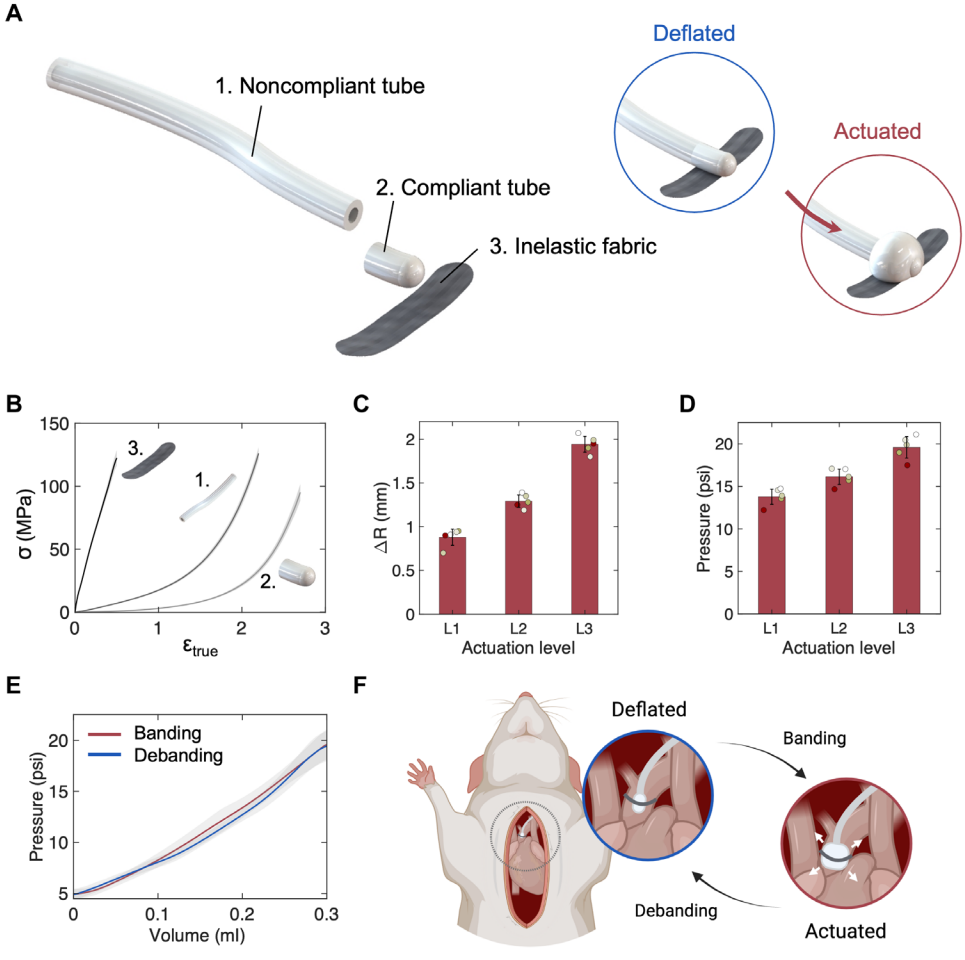


**Fig. 1. Design overview and mechanical characterization of soft robotic actuator.** (**A**) Components of the soft robotic actuator, highlighting the noncompliant and compliant tubing and the inelastic fabric sheet. Illustration of the compliant tubing in the deflated and actuated states. (**B**) Stress-strain behavior of the materials constituting the actuator ($n = 5$ for each material), where σ and $\varepsilon_{true}$ indicate the Cauchy stress and the true strain, respectively, of each material under uniaxial tension. (**C**) Maximum radius and (**D**) pressure at three distinct actuation levels (L1 to L3). (**E**) Pressure-volume curves during banding and debanding. (**F**) Illustration of the actuator positioned around the ascending aorta of a rat model. Illustration of the expansion of the implanted actuator during aortic banding and debanding. Data show means ± 1 SD. Each test was conducted on $n = 5$ actuators and repeated $n = 5$ times.

The design and the behavior of the device were optimized to enable in vivo implantation around the ascending aortas of the animals, allowing for controlled, progressive, and reversible banding. The position of the device on the ascending aorta and changes to the diameter of the actuator during banding and debanding are illustrated in Fig. 1F.

### Modulation of cardiac hemodynamics at distinct levels of aortic banding and debanding

We demonstrated the controllability of the actuator in an acute rat model through invasive hemodynamic monitoring of LV function. Figure 2A shows representative LVP and aortic pressure (AoP) waveforms over four consecutive heartbeats at baseline, at three distinct levels of actuation (L1 to L3), and at return to baseline after debanding. Elevations in LVP and a reduction in the amplitude (pulse) of the AoP are consistent with hemodynamic changes associated with pressure overload. Through constant-rate volume-control pressurization of the soft robotic actuator, we could visualize progressive hemodynamic changes during banding and debanding. Changes in LVP and AoP over actuation are shown in Fig. 2B. Analogously, the progression of the LV pressure-volume loop during banding is depicted in Fig. 2C, highlighting elevations in LVP and a drop in the stroke volume due to banding.

Figure 2 (D to I) shows progressive changes in parameters of LV function for each actuation level during both banding and debanding. For the lowest and highest levels of actuation, respectively, aortic banding resulted in an increase in $LVP_{max}$ (21.0 to 107.6%; Fig. 2D), a drop in cardiac output (−1.5 to −29.3%; Fig. 2E), and an increase in stroke work (17.7 to 68.2%; Fig. 2F). Aortic banding also caused an increase in the end-systolic volume (Fig. 2G) and in the end-diastolic volume (Fig. 2H), leading to an overall drop in stroke volume (−1.4 to −31.0%; Fig. 2I).

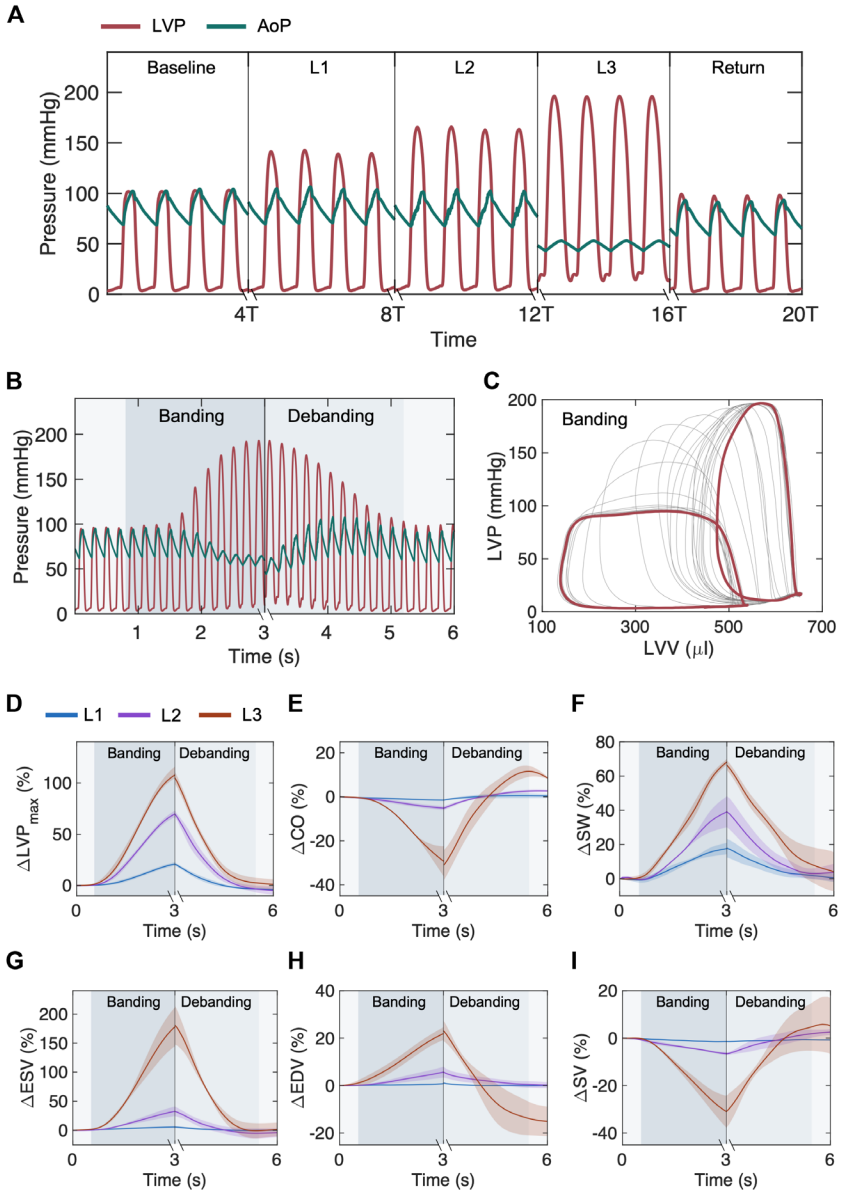


**Fig. 2. Modulation of cardiac hemodynamics during acute aortic banding and debanding in acute catheterization study.** (**A**) Representative LV and AoP waveforms at baseline, L1 to L3, and return to baseline after debanding. (**B**) Representative progression of LV and AoP during banding and debanding. (**C**) Changes in the LV pressure-volume loop during banding. Highlighted loops correspond to baseline and peak banding. (**D** to **I**) Relative changes in cardiac function during banding and debanding for three actuation levels, including (D) maximum LVP, (E) cardiac output, (F) stroke work, (G) end-systolic volume, (H) end-diastolic volume, and (I) stroke volume. Data show means ± 1 SD. Each test was conducted on $n = 5$ animals and repeated $n = 3$ times.

In this acute demonstration of our platform, all metrics of cardiac function (Fig. 2, D to I) were calculated at peak banding, before physiologic compensation to pressure overload. Debanding was then performed 3 to 5 s after peak banding. Although all metrics showed a reversal of the acute changes induced by aortic constriction, SDs were generally higher in the return state than at baseline. These changes were particularly notable after the most severe level of banding (L3), likely because of differences in the tolerance of severe aortic constriction among different animals.

### MRI and catheterization studies showed recapitulation of the hemodynamics of AS and reversal

We visualized the aortic cross section and characterized changes in the blood velocity profile using MRI. Figure S1A summarizes the analysis workflow from phase-contrast MRI data to allow for flow visualization on two-dimensional (2D) velocity maps. Figure 3A illustrates the soft robotic actuator, aortic cross sections, and corresponding 2D velocity maps at baseline and for mild, moderate, and severe banding. Images show that the actuator progressively constricts the aorta at increasing levels of banding. Correspondingly, the peak blood flow velocity at the constriction increased from 1.1 m/s at baseline to 4.5 m/s at severe constriction as a result of progressive banding. The 2D aortic velocity profiles due to acute aortic banding on $n = 3$ animals are shown in fig. S1B.

Changes in the orifice area, peak blood flow velocity, and aortic hemodynamics due to banding and debanding for L1 to L3 were comprehensively characterized using catheterization techniques (Fig. 3, B to G). For this approach, we inserted two pressure-volume catheters into the LV, advancing one into the aortic arch through the area of aortic constriction. Progressively, from L1 to L3, we observed a drop in the orifice area (−45.0 to −74.2%; Fig. 3B) and an increase in the mean (26.6 to 81.3 mmHg; Fig. 3C) and maximum transaortic pressure gradients (47.2 to 127.3 mmHg; Fig. 3D) and the maximum flow velocity (3.4 to 5.6 m/s; Fig. 3E). Further, the energy loss index decreased (Fig. 3F), and the valvulo-arterial impedance increased (Fig. 3G). Akin to the changes in cardiac function (Fig. 2, D to I), changes in each of these metrics were acutely reversed because of debanding, with greater variability in the return state than at baseline, likely due to differences in hemodynamic compensation to pressure overload.

### Platform versatility for various banding and debanding modalities

Figure 4 demonstrates the control of pressure overload that can be achieved using the soft robotic actuator through stepwise and prolonged hold actuation studies via measurements of LVP and AoP (Fig. 4, A and B); mean and maximum transaortic pressure gradient (Fig. 4, C and D); cardiac output (Fig. 4, E and F); and stroke volume, end-diastolic volume, and end-systolic volume (Fig. 4, G and H). The stepwise banding and debanding studies were conducted in steps of 0.02 ml of actuation medium and showed consistent trends in changes of metrics of LV and aortic hemodynamics, as demonstrated previously (Figs. 2, A, E, and G to I, and 3, C and D). Stepwise banding resulted in progressive elevations in systolic LVP, a drop in AoP (Fig. 4A) and in mean and maximum transaortic pressure gradient (Fig. 4C), and a progressive drop in cardiac output (Fig. 4E) and stroke volume (Fig. 4G). Changes in LVP and AoP during stepwise debanding were opposite but lesser in magnitude than during banding, likely because of complex compensation dynamics (Fig. 4, A and C). Compensatory mechanisms, including the Frank-Starling law, sympathetic up-regulation, and neurohormonal activation, during stepwise actuation could also be observed by the increase in cardiac output and stroke volume at peak banding (Fig. 4, E and G). Stepwise debanding caused the end-diastolic volume and end-systolic volume to return to baseline, fully restoring baseline values of cardiac output and stroke volume (Fig. 4, E and G).

The prolonged hold study was performed to demonstrate the ability of the actuator to remain inflated over time. Figure 4B shows representative LVP and AoP waveforms over ~20 min. Associated sustained changes in mean and maximum transaortic pressure gradient (Fig. 4D); cardiac output (Fig. 4F); and stroke volume, end-diastolic volume, and end-systolic volume (Fig. 4H) are consistent with findings in the acute study. Further, the gradual increase in cardiac output and stroke volume in Fig. 4(F and H) highlights the onset of compensatory mechanisms because of prolonged hold. These results supported the use of our model for controlled, progressive, and reversible aortic constriction in the chronic setting.

### MRI evaluation of proof-of-concept chronic study of progressive pressure overload and reversal

We designed a proof-of-concept chronic study to showcase the feasibility of the proposed model for long-term studies of aortic banding and cardiac remodeling as well as of its tunability and versatility. We implanted the actuator in a total of $n = 9$ Sprague-Dawley female rats. In the control group ($n = 3$), the actuator was implanted but never actuated. In the remaining $n = 6$ rats, the degree of aortic constriction was progressively increased over the course of 3 weeks. At the 3-week time point and for 2 additional weeks, the maximal level of aortic banding was then maintained in the banding group ($n = 3$), whereas it was reversed in the banding + debanding group ($n = 3$). The progressive levels of pressure overload in the banding and banding + debanding groups are shown in Fig. 5A. Hematoxylin and eosin (H&E) images in fig. S2 show that chronic implantation of the actuator did not result in any notable inflammatory response of the aortic tissue at the 5-week time point, supporting the suitability of long-term studies. The tissue appeared to have normal morphology, with an absence of typical inflammatory features, such as infiltration of inflammatory cells (e.g., lymphocytes, macrophages, and plasma cells), fibrosis, or tissue necrosis. Changes in LV structure and function in all animals were evaluated weekly via MRI for a total of 5 weeks after implantation. Histological analysis of aortic and LV tissue was conducted on sacrifice. A pilot MRI study ruled out changes in cardiac function or structure because of sole actuator implantation (fig. S3).

Figure 5B illustrates variations in the aortic cross section (or anatomical valvular area) across the three groups. At week 3, the actuated groups showed an average reduction in aortic cross section of −51.2%. At weeks 4 and 5, this drop was maintained in the banding group, whereas it was reversed in the banding + debanding group. Representative MRI anatomical images of the aortic cross section in short-axis view are shown in Fig. 5C. This highlighted the progressive increase in the actuator cross-sectional area and the subsequent drop in aortic cross section from baseline to severe actuation. These changes were then reversed at week 5 in the banding + debanding group. At each time point, corresponding short-axis images of the LV are also shown. Changes in the interventricular septum, posterior wall, and free wall thickness were measured via MRI throughout the study as indicative of LV remodeling due to pressure overload. Figure 5C highlights the thickening of the LV wall from baseline to week 3 and

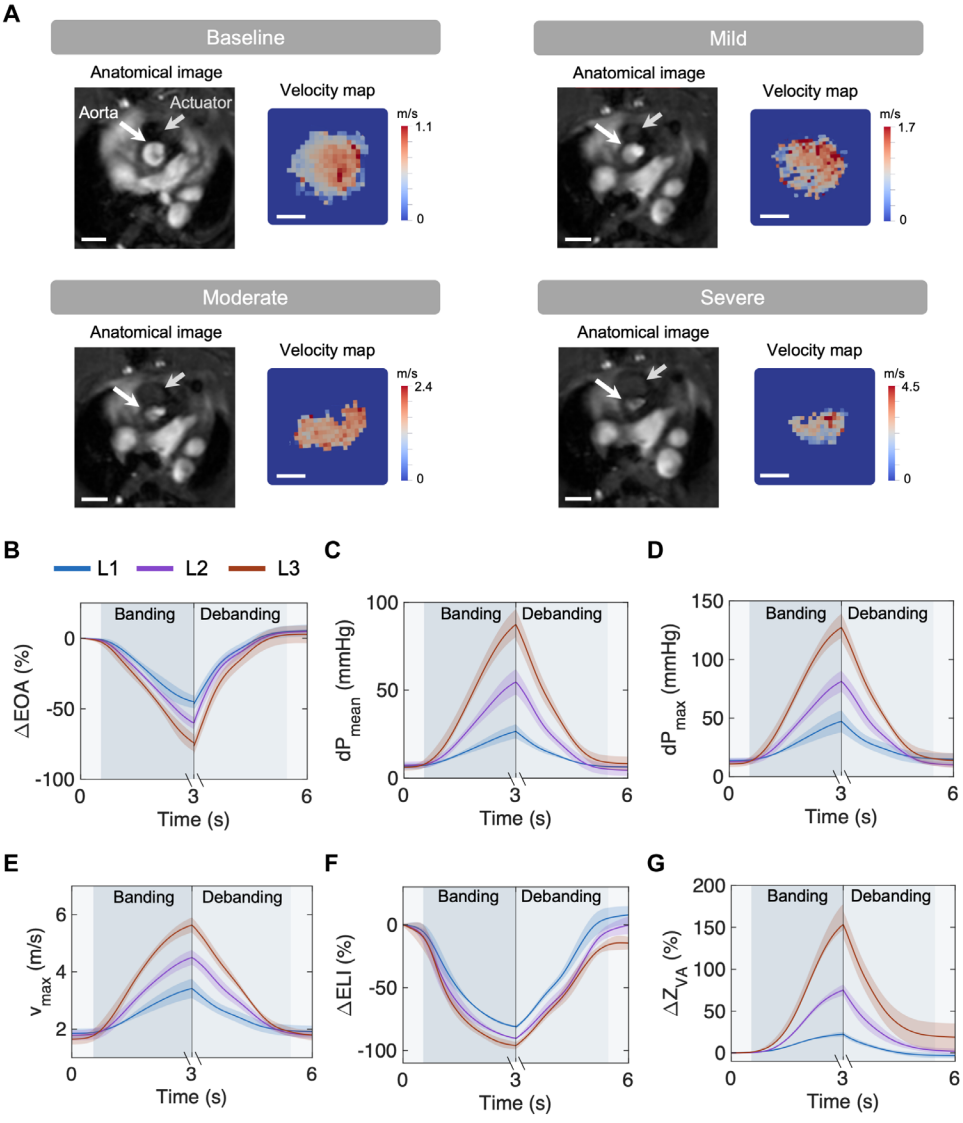


**Fig. 3. Aortic hemodynamics during acute aortic banding and debanding.** (**A**) Representative cross-sectional images of the actuator and aorta with corresponding 2D aortic velocity maps at baseline and distinct actuation levels. Scale bars, 3 mm on anatomical images and 1 mm on velocity maps. (**B** to **G**) Changes in aortic hemodynamics measured via catheterization during banding and debanding for three actuation levels (L1 to L3), including (B) effective orifice area, (C) mean transaortic pressure gradient, (D) maximum transaortic pressure gradient, (E) maximum velocity, (F) energy loss index, and (G) valvulo-arterial impedance. Data show means ± 1 SD. Each test was conducted on $n = 5$ animals and repeated $n = 3$ times.

reversal to baseline at week 5 due to debanding. Representative M-mode images of the LV as well as pulse-wave and color Doppler imaging of blood flow through the actuator obtained using ultrasound at various degrees of aortic banding are shown in fig. S4.

Quantitatively, Fig. 5 (D to F) illustrates changes in LV wall thickness throughout the 5-week study with respect to baseline. At peak banding, the interventricular septum (Fig. 5D), free wall (Fig. 5E), and posterior wall (Fig. 5F) thickness increased significantly in the actuated groups. In the banding group, these increased progressively through week 5, whereas they dropped because of debanding. At week 5, there was no significant difference in LV wall thickness between the control and the banding + debanding groups, indicating that these remodeling processes may be reversible if the pressure overload is relieved. Figure 5 (G to I) shows that progressive aortic banding resulted in a progressive drop in end-diastolic volume (Fig. 5G). Because aortic banding did not cause significant changes in end-systolic volume (Fig. 5H), the stroke volume dropped significantly in these groups (Fig. 5I). In the banding + debanding group, these changes were found to be reversed. Further, an upward trend could be observed in most anatomical metrics in the control group, likely because of the animals' own growth throughout the study. No statistically significant change in LV ejection fraction was observed between the start and end of the study in any group (fig. S5A). All structural and functional data measured at baseline are reported in table S1.

## Histologic evaluation of progressive pressure overload and reversal in chronic model

Gross anatomic and histologic examination of key organs was conducted after animal sacrifice. We evaluated the heart, lung, and kidney weight–to–tibial length ratios across the three groups (Fig. 6, A to C). All three ratios were moderately increased in the banding group compared with control, whereas no statistically significant difference was observed between the banding + debanding group and the control. Tibial length variability between the animals in this study is reported in table S1. Changes in body weight during the study indicated no significant difference between the groups (fig. S5B).

As a result of banding, the mean cardiomyocyte volume-weighted mean volume in the myocardium (Fig. 6D) and the mean cell width in the subendocardium (Fig. 6E) were elevated compared with control. Consistent with changes in LV structure and function measured on MRI (Fig. 5, D to I) and with measurements of organ weight (Fig. 6, A to C), these changes in cardiomyocyte volume and width were partially reversed in the banding + debanding group. Representative H&E images of the myocardium and subendocardium in the three groups are shown in Fig. 6F and fig. S5C, respectively.

Measurements of the total interstitial (Fig. 6G) and perivascular (Fig. 6H) fibrosis volume fraction show a trend toward increased fibrosis in the banding group compared with control. Measurements of interstitial and perivascular fibrosis in the myocardium and subendocardium, individually, show analogous trends (fig. S5 D to G). Representative images of the myocardium

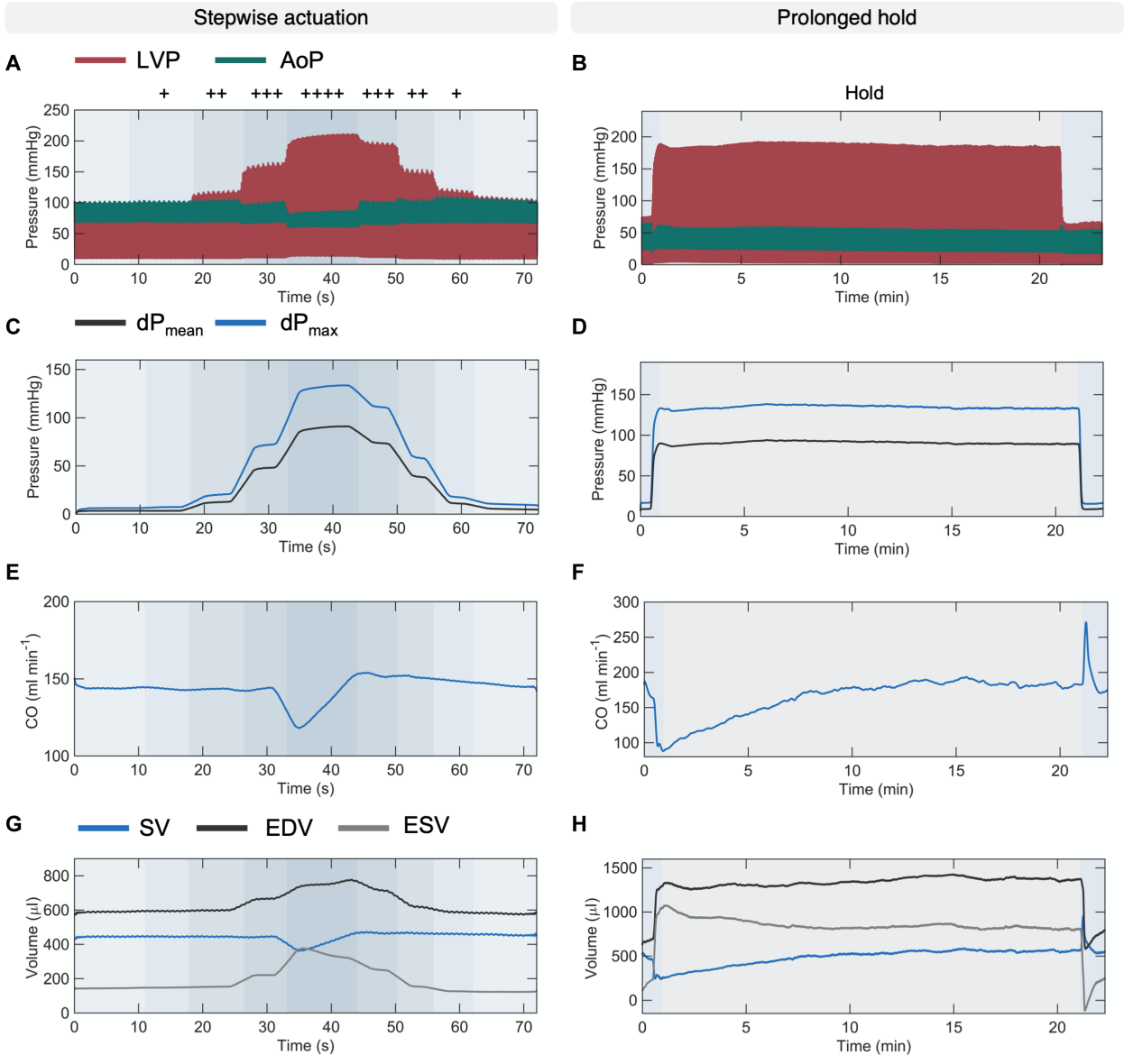


**Fig. 4. Stepwise and prolonged actuation studies.** (**A** to **H**) Evolution of metrics of cardiac function and aortic hemodynamics during a stepwise and prolonged hold actuation studies, showing (A) LV and (B) AoP waveforms; (C and D) mean and maximum transaortic pressure gradient; (E and F) cadiac output; and (G and H) stroke volume, end-diastolic volume, end-systolic volume. Actuation volumes: 0.24 ml (+), 0.26 ml (++), 0.28 ml (+++), and 0.3 ml (++++).

(Fig. 6I) and subendocardium (fig. S5H) stained with picrosirius red illustrate differences in the interstitial and perivascular fibrosis across the three groups.

## DISCUSSION

This work describes an implantable soft robotic actuator for the development of a highly tunable, small-animal model of LV pressure overload. By relying on an actuatable material that can achieve controlled, progressive, and reversible aortic banding in a rat model, this platform overcomes several of the limitations associated with other preclinical models of disease, such as lack of tunability of the degree of pressure overload and the subsequent inability to recapitulate the natural progression of disease or reversal due to medical intervention.

The soft actuator is composed of a compliant tube that expands under pressure (Fig. 1A). Its expansion can be controlled by tuning the actuation volume, which results in predictable changes in the diameter and pressure of the actuator (Fig. 1, C to E). This soft robotic actuator could achieve a maximum expansion area of ~15 $mm^2$, allowing for controlled constriction of the ascending aorta of a wide range of animal sizes and, potentially, for a broader spectrum of applications. In terminal studies, we used invasive hemodynamic monitoring to measure metrics of cardiac function (Fig. 2) and aortic hemodynamics (Fig. 3) during progressive banding and debanding for discrete actuation levels. We obtained LV pressure-volume

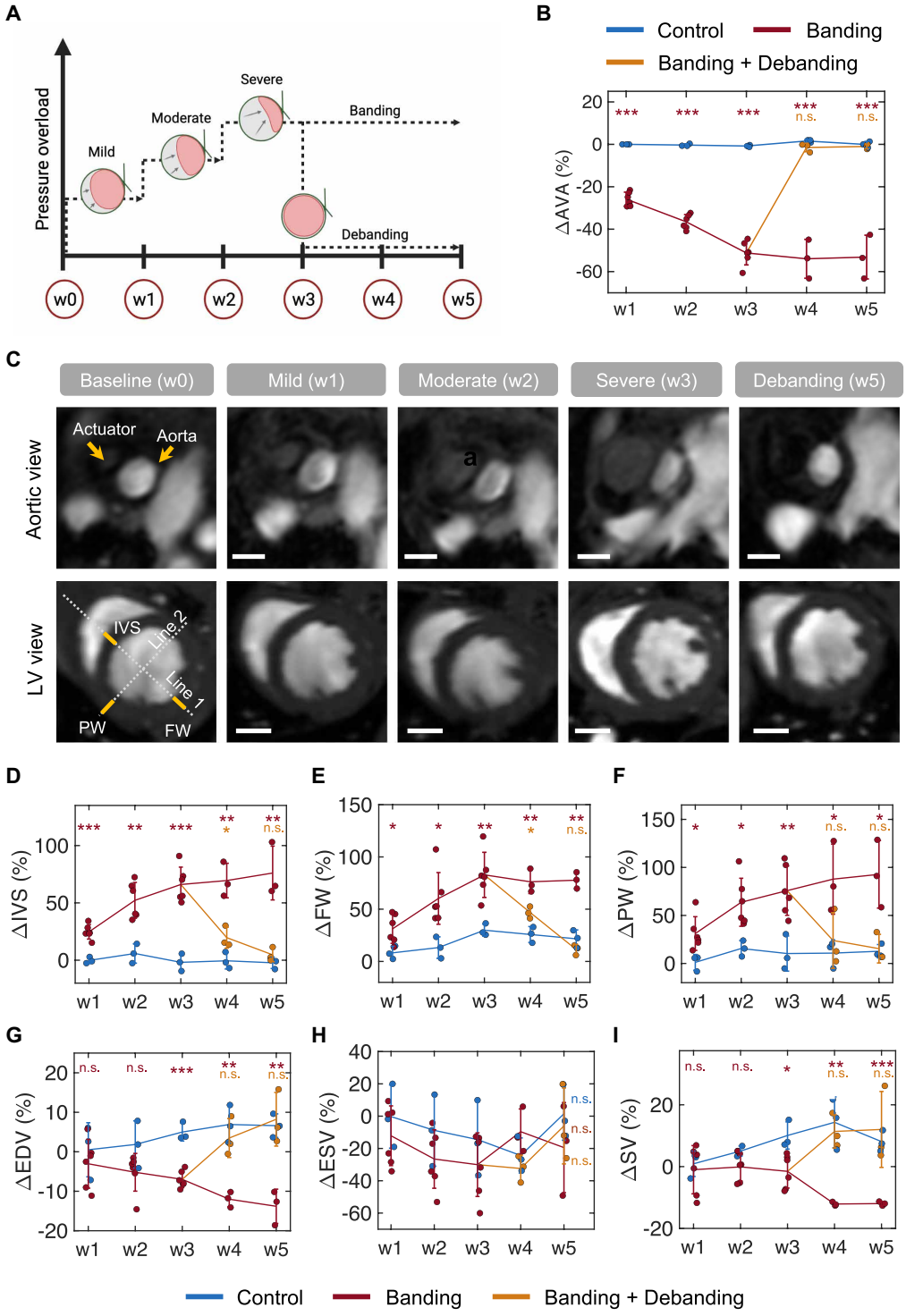


**Fig. 5. MRI study of chronic cardiac remodeling and reversal via progressive banding and debanding.** (**A**) Overview of the timeline of the proof-of-concept chronic studies and levels of pressure overload. (**B**) Changes in aortic cross section measured weekly throughout the study. (**C**) Representative anatomical images of the aorta and left ventricle in short-axis view for various levels of banding. Lines 1 and 2 indicate the geometrical constructions used to obtain wall thickness values. Scale bars, 2 mm. (**D** to **F**) LV structural changes over time, including (D) interventricular septum, (E) free wall, and (F) posterior wall thickness. (**G** to **I**) Changes in metrics of LV function over time, including (G) end-diastolic volume, (H) end-systolic volume, and (I) stroke volume. $n = 3$ in each group; $n = 6$ in banding group weeks 1 to 3. $^{*}P < 0.05$; $^{**}P < 0.01$; $^{***}P < 0.001$; n.s., nonsignificant.

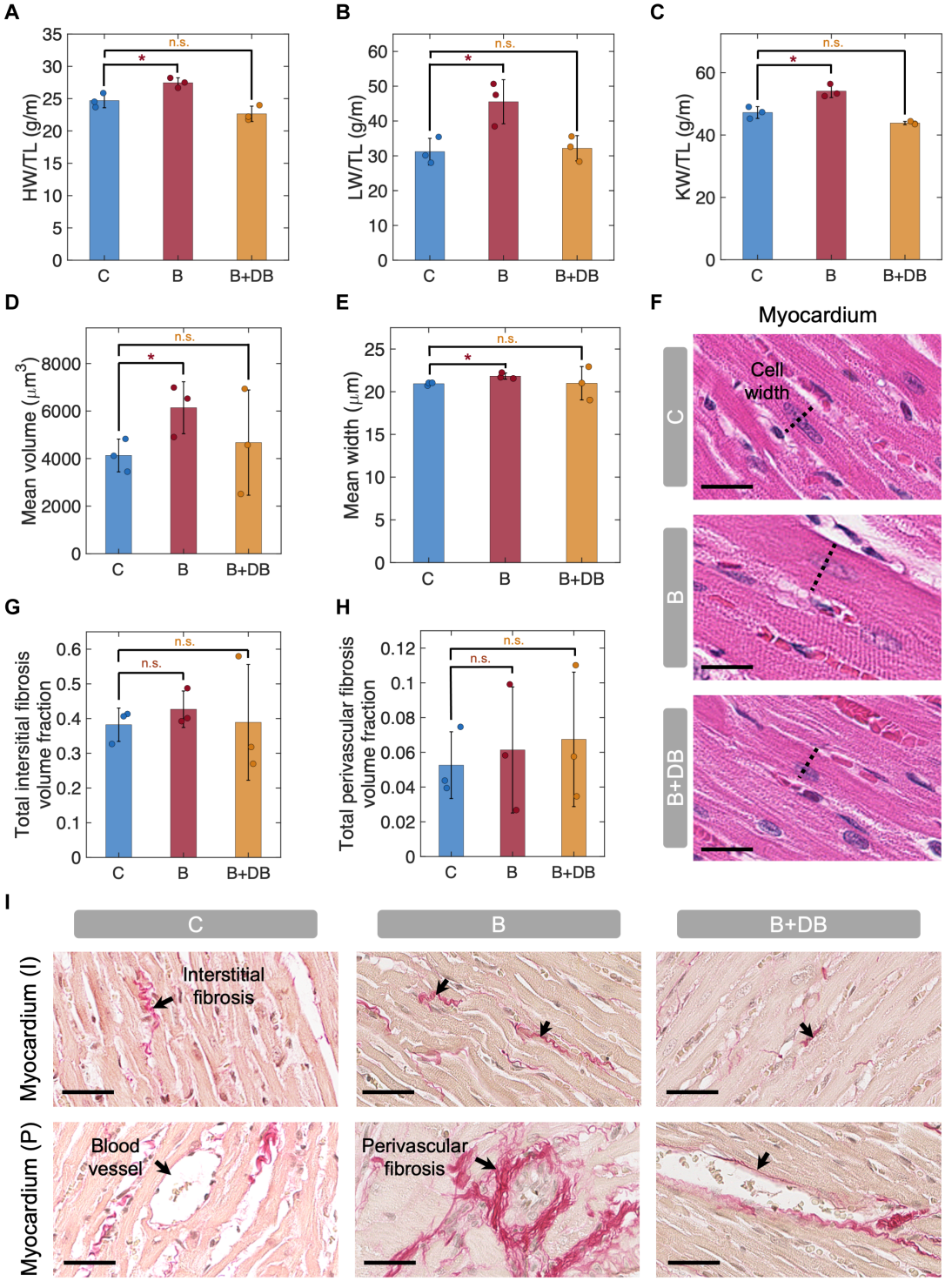


**Fig. 6. Organ weight measurements and histology analysis.** (**A** to **C**) Organ weight to tibial length (TL) ratio, including (A) heart (H), (B) lung (L), and (C) kidney (K). (**D** to **F**) LV cardiomyocyte analysis, showing (D) volume-weighted mean volume of cardiomyocytes in the myocardium, (E) mean cell width in subendocardium, and (F) representative myocardium H&E slides. Scale bars, 20 μm. (**G** to **I**) Fibrosis evaluation, showing (G) total interstitial and (H) perivascular fibrosis volume fraction and (I) representative picrosirius red images, highlighting myocardial interstitial and perivascular fibrosis. Scale bar, 40 μm. $n = 3$ in each group; $n = 6$ in banding group weeks 1 to 3. *$P < 0.05$.

loops (Fig. 2C) and measured $LVP_{max}$ (Fig. 2D), cardiac output (Fig. 2E), stroke work (Fig. 2F), and LV volumes (LVVs; Fig. 2, G to I). We calculated diagnostic metrics of AS, such as effective orifice area (Fig. 3B), transaortic pressure gradient (Fig. 3, C and D), maximum velocity (Fig. 3E), energy loss index (Fig. 3F), and valvuloarterial impedance (Fig. 3G), and characterized changes in LV and aortic hemodynamics during stepwise and prolonged actuation studies (Fig. 4). Changes in these metrics demonstrated the ability of the system to induce various levels of aortic banding and to return to the original hemodynamic state via debanding. Although the actuator allows precise control over aortic constriction, the hemodynamic responses vary among animals because of a complex interplay of regulatory mechanisms responding to increased afterload. Further analysis into compensatory mechanisms would require a series of studies specifically designed to isolate and investigate each variable independently, which can be enabled by the proposed platform.

In this work, MRI was leveraged to directly visualize the degree of aortic constriction due to the soft actuator. Although small measurement variations may arise because of potential differences in animal positioning and MRI slicing between distinct scans, overall, MRI reduces measurement variability due to operator experience associated with echocardiography (*31*, *32*). Further, MRI allowed us to visualize blood flow through the aortic constriction (Fig. 3A and fig. S1), which could be key in future studies of shear and vortex formation and their effects on disease progression (*29*).

We then demonstrated the potential of the proposed disease model for long-term studies of pressure overload through a proof-of-concept 5-week investigation. The actuator was used to achieve progressive aortic banding, through three distinct levels, for 3 weeks. The level of pressure overload was then maintained for 2 additional weeks in a subset of animals, whereas it was reversed to baseline in another subset (Fig. 5A). Weekly MRI studies were used to quantify the degree of aortic constriction (Fig. 5B) as well as structural changes in the LV due to remodeling (Fig. 5, C to F). Consistent with the literature, which reports a 30 to 60% increase in the interventricular septum thickness and an ~50% increase in posterior wall thickness (*12*, *33*), our model resulted in a 66 to 76% and a 76 to 93% increase in interventricular septum and posterior wall thickness, respectively (Fig. 5, D and F), 3 to 5 weeks after debanding. In addition, we observed that, after 3 weeks of banding, changes in LV wall thickness are almost completely reversible (80 to 90% reduction) 2 weeks after debanding (Fig. 5, D and F). Other studies have shown analogous results, with a 60 to 70% drop in interventricular septum thickness 2 weeks after debanding after 5 weeks of banding (*33*). Although previous investigations of cardiac remodeling reversal required invasive removal of the aortic clip or suture (*19*, *25*–*27*), using our soft robotic approach, debanding studies could be conducted without any additional surgeries.

These findings were consistent with the changes in cardiac function measured via MRI, organ weight, and histology. Thickening of the LV resulted in a progressive (and reversible) drop in the end-diastolic volume (Fig. 5G) and stroke volume (Fig. 5I), whereas no changes in LV ejection fraction were observed during this study (fig. S5A). An assessment of heart, lung, and kidney weights showed a moderate increase in the banding group compared with control (Fig. 6C). Histological findings highlighted an ~50% increase in the mean cardiomyocyte volume (Fig. 6D) due to aortic banding. Analogously, the total (myocardial and subendocardial) interstitial (Fig. 6G) and perivascular (Fig. 6H) volume fractions increased roughly by 12 and 17%, respectively, in the banding group. At the 5-week time point, perivascular fibrosis did not exhibit significant reversal due to debanding, which is likely because of a potentially slower process compared with the reversal of interstitial fibrosis and cardiomyocyte size.

This study has some limitations. Implantation of a soft robotic actuator around the ascending aorta of a small animal is challenging and requires good surgical skills. The additional difficulties associated with these surgeries may explain the relatively high postoperative mortality rates (40%). In our study, all deaths could be attributed to decompensation because of acute pericarditis developed 8 to 12 days after operation, as confirmed by autopsy or MRI studies. We hypothesize that the pericarditis may be a direct consequence of the surgery or friction between the actuator and the pericardium. Nevertheless, the ability to control the degree of pressure overload could reduce mortality by enabling gradual progression to severe aortic constriction and by enabling aortic debanding to allow for animal recovery. Further, a more comprehensive characterization of the degree of LV remodeling and its reversal needs to be conducted for various levels of aortic constriction and durations of debanding. These studies could shed light on ventricular plasticity and the optimal time of intervention to halt or reverse remodeling, restoring adequate cardiac mechanics and hemodynamics. Clinically, they could affect management strategies for patients with cardiac remodeling secondary to AS or hypertension (*34*–*36*).

The integration of sensing capabilities and closed-loop feedback with the design of the soft robotic actuator would allow us to achieve the desired amount of aortic constriction in an automated manner. This advancement would enhance the precision and reliability of our model, allowing for real-time adjustments to maintain specific levels of aortic constriction, further mimicking the dynamic nature of cardiovascular diseases. In addition, we plan to investigate the integration of the proposed model with current strategies to co-induce HFpEF comorbidities (*37*–*39*), as well as the long-term modulation of pressure overload to mitigate the risk of transition to phenotypes other than HFpEF (*14*, *15*). If successful, these studies could further elucidate the interplay between mechanical and biological stressors and further contribute to the establishment of a more clinically relevant small-animal model of HFpEF.

Ultimately, the ability to recapitulate and control multiple aspects of disease may lead to the development of more accurate models of human physiology and disease. These models could play a critical role in allowing us to elucidate mechanisms of disease not yet fully understood and to develop more effective treatments for patients affected by these conditions. This work may pave the way toward the design of highly tunable models of disease within and beyond the cardiovascular space, providing a toolset to improve current methods for fundamental and preclinical research.

## MATERIALS AND METHODS

### Study design

The in vivo study of this work was composed of three main phases, namely, acute hemodynamic evaluation via catheterization and aortic flow velocity maps, chronic animal model development and structural and functional evaluation on MRI, and tissue remodeling analysis via histology studies. This study aimed to demonstrate the ability of the actuator to recapitulate the hemodynamics of LV pressure overload in a tunable and reversible manner and to evaluate

changes in cardiac function and structure and their reversal, due to progressive aortic banding and debanding. For all studies, sample size determination was based on a power analysis to ensure adequate power to detect a statistically significant difference, with an α value of 0.05 and a power of 0.80.

### Actuator characterization

The mechanical properties of the materials constituting the soft robotic actuator were measured under uniaxial tensile loading using a 2-kN load cell on an electromechanical tester (Instron 5566, MA). A strain rate of 0.05 per second, corresponding to 0.75 mm/s for a gauge length of 15 mm, was used for mechanical testing because it is analogous to a deformation rate (~0.8 mm/s) of the actuator during the in vivo studies. The fabric sheet was cut to a width of 2.7 mm. The sheet had a thickness of 0.2 mm, and the tubes preserved their original ID and OD dimensions. Uniaxial tensile testing was conducted to failure on $n = 5$ specimens for each material. The raw force-displacement data were converted to the Cauchy stress ($\sigma$) and true strain ($\varepsilon_{true}$) using Eqs. 1 to 3

$$\varepsilon_{eng} = \frac{l - l_0}{l_0} \tag{1}$$

$$\varepsilon_{true} = \ln(1 + \varepsilon_{eng}) \tag{2}$$

$$\sigma = \frac{F}{A}(1 + \varepsilon_{eng}) \tag{3}$$

where $\varepsilon_{eng}$, $\varepsilon_{true}$, and $\sigma$ indicate the engineering strain, the true strain, and the true (or Cauchy) stress, respectively; $F$ and $l$ are the force and the displacement applied to the sample; and $A$ and $l_0$ are the initial cross-sectional area and the initial length of the sample. The Young's modulus, $E$, of the fabric was calculated as the slope of the stress-strain curve in the $\varepsilon_{true} = 0$ to 0.5 interval. The stress-strain response of the tubes was fitted using the simplified Ogden model (*40*) in Eqs. 4 and 5

$$\lambda = \frac{l}{l_0} \tag{4}$$

$$\sigma = a\,(\lambda^b - \lambda^{-\frac{b}{2}}) \tag{5}$$

where $\lambda$ is defined as the stretch in the uniaxial direction and $a$ and $b$ are the parameters of the equation. All data were plotted up to failure point.

Changes in the pressure and expansion of the actuator during banding and debanding were measured by adding up to 0.3 ml of medium (glycerin, $\rho = 1.26$ g/cm$^3$; $\nu = 11.10$ mPa·s) using a syringe pump (70–3007 PHD ULTRA Syringe Pump Infuse/Withdraw, Harvard Apparatus, MA) at a constant rate of 0.1 to 0.2 ml/s. Volumes of 0.26, 0.28, and 0.3 ml were infused during testing at discrete actuation levels corresponding to levels L1 to L3. The pressure inside the actuator was measured using the PS-3203 wireless pressure sensor (PASCO, CA). Changes in diameter were recorded using a camera system oriented perpendicularly to the actuator. Images were processed using ImageJ for Mac OS X.

### Implantation for in vivo studies

All animal procedures were reviewed and approved by the Institutional Animal Care and Use Committee of the Massachusetts Institute of Technology. Sprague-Dawley female rats were used (average body weight of 241.8 ± 11.5 g). Before surgery, all animals were anesthetized using 2 to 4% isoflurane. After weighing, sterile eye ointment was applied, and the backs and chests of the animals were shaved. For survival studies, preoperative antibiotic and analgesic medications were administered, including enrofloxacin (10 mg/kg, intramuscular), buprenorphine (1.0 to 1.2 mg/kg, subcutaneous), meloxicam (2 mg/kg, subcutaneous), and lidocaine (5 to 10 mg/kg, subcutaneous). All surgical tools were autoclaved before survival surgeries. Endotracheal intubation was performed to allow mechanical ventilation (2.5 ml per breath at 70 breaths per minute). Temperature support was provided with an electric heating pad during the surgery.

The soft robotic actuator was implanted via sternotomy or left thoracotomy at the fourth intercostal space for terminal and survival procedures, respectively. Careful dissection of the muscle layers was performed before placement of a self-retaining retractor to allow better visualization of and access to the ascending aorta. The ascending aorta could then be identified and carefully isolated. The actuator was therefore wrapped loosely around the ascending aorta and then tightened by creating a double knot with the fabric sheet. The noncompliant tubing was tunneled out of the chest wall through a small incision in the third intercostal space and into the lateral subcutaneous space. The intercostal spaces were then closed using several interrupted 4-0 Vicryl sutures. A fenestrated flexible 24-gauge catheter connected to a 5-ml syringe was inserted in the chest cavity through the thoracotomy, and suction was applied to restore negative pressure in the thorax during a breath-hold before the final suture was tied town. The inflexible tubing was tunneled above the left forelimb to the left anterior chest above the forelimb. A counterincision was made in the skin in preparation for tunneling to the dorsum, and the port for the tubing was secured in the subcutaneous tissue. The subcutaneous and skin layers of the thoracotomy incision were then closed with Vicryl as above.

For placement of the percutaneous port for survival surgeries, the rat was turned to the prone position, and a small incision (1 to 2 cm) was made between the shoulder blades of the animal after sterile preparation of the surgical site. The tubing of the device was grasped with forceps through the lateral counter incision and then tunneled through the dorsal side. An MRI-safe vascular access button (VAB62SMBS/25-MRI or VAB95BS-MRI, Instech Laboratories, PA) was connected to the distal end of the tubing and placed subcutaneously between the shoulder blades of the rat. The tubing was finally secured with a 5-0 nylon suture to the port. The skin incisions were then closed with 5-0 nylon and skin glue.

After the procedure, the isoflurane was decreased to 1%, and the ventilator was turned off while the animal was monitored for spontaneous breathing. After return to normal respiration, the isoflurane was turned off. The animals were then extubated. For survival procedures, meloxicam (2 mg/kg, oral) and enrofloxacin (2-mg tablets, oral) were administered at 24 and 48 hours after surgery.

### Cardiac and aortic catheterization

For terminal catheterization, a median sternotomy was used for the surgical approach as detailed above. Invasive hemodynamic measurements were obtained using two 2-French straight pressure-volume catheters (SPR-838, Millar, TX) that were inserted in the LV and aorta via LV puncture with a 27-gauge needle. The catheters were connected to the MPVS Ultra console (Millar, TX), which was, in turn, connected to the Powerlab system (PowerLab 8/26, ADInstruments, Australia) for monitoring and acquisition. The data were displayed and recorded in real time on LabChart (Pro v8.1.16, ADInstruments). A sampling frequency of 1000 Hz and a band-stop filter at 50 Hz were used.

LV and aortic characterizations were conducted on $n = 5$ rats. LV and aortic hemodynamics during the prolonged and stepwise actuation studies were measured on a subset of $n = 3$ rats per group. Steps of 0.01 to 0.02 ml of medium were used to progress from one actuation level to the other (L1 to L3) for each study, using a syringe pump (Harvard Apparatus) at a rate of 0.1 to 0.2 ml/s. After invasive hemodynamic evaluations, the rats were euthanized by aortic transection under anesthesia.

### Calculation of AS hemodynamic metrics

Metrics of AS during catheterization studies were calculated using standard equations. The Gorlin equation was used to compute the effective orifice area (EOA) (Eq. 6) (*41*)

$$\mathrm{EOA} = \frac{Q}{\mathrm{BSA}\ 51.6\ \sqrt{\Delta P_{\mathrm{mean}}}} \tag{6}$$

where $Q$ is the aortic flow, BSA is the body surface area of the animal, and $\Delta P_{\mathrm{mean}}$ is the mean transaortic pressure gradient, as measured with the LV and aortic catheters.

The maximum velocity ($v_{\mathrm{max}}$) was estimated from pressure-volume measurements of the transaortic pressure gradient (Eq. 7) (*42*)

$$v_{\mathrm{max}} = \sqrt{\frac{\Delta P_{\mathrm{max}}}{4}} \tag{7}$$

The energy loss index (ELI) was calculated using Eq. 8 (*43*)

$$\mathrm{ELI} = \frac{\mathrm{EOA}\ (A_{\mathrm{a}})}{\mathrm{BSA}(A_{\mathrm{a}} - \mathrm{EOA})} \tag{8}$$

where $A_{\mathrm{a}}$ is the cross-sectional area of the aorta measured at the sinotubular junction.

The valvulo-arterial impedance was measured using Eq. 9 (*44*)

$$Z_{\mathrm{VA}} = \frac{\mathrm{LVP}_{\mathrm{max}}}{\mathrm{SV}}\mathrm{BSA} \tag{9}$$

where $\mathrm{LVP}_{\mathrm{max}}$ is the peak systolic LVP and SV is the stroke volume, as obtained from LV catheterization.

In these equations, the BSA was estimated from the body weight (BW) of the rat using the Rubner formula (*45*) (Eq. 10)

$$\mathrm{BSA} = 9.46\ (\mathrm{BW})^{\frac{2}{3}} \tag{10}$$

### MRI data acquisition

MRI was performed in vivo on a 7-T MRI operated by Bruker AV4 NeoBioSpec70-20USR console, equipped with a 114-mm 660-mT/m actively shielded gradient (Bruker BioSpin, Rheinstetten, Germany) and a 63-mm-ID Varian volume RF coil (Agilent Technologies). Rats were anesthetized by inhalation of 3% isofluorane and maintained on 2 to 2.5% isofluorane throughout data collection. Body temperature, respiration rate, and the electrocardiogram (EKG) signal were observed via a monitoring and gating system (Small Animal Instruments Inc., Stony Brook). All data were collected and reconstructed within Bruker Paravision PV360 v2.0 and converted to DICOM format.

Slice position was determined on the basis of the Localizer and Planning protocols. Quantitative flow maps of the aorta were acquired using the Velocity Map protocol with values of time to echo to repetition time (TE/TR) = 5/30 ms, three averages, and a flip angle of 40° in the slice direction. The velocity encoding (VENC) value was adjusted on the basis of estimated aorta flow rates, ranging from 110 to 500 cm/s. A field of view of 40 mm by 40 mm, an in-plane data matrix 256 by 256, and a slice thickness of 0.7 mm with no gap were used for this study. Triggering was turned on per slice for both EKG and respiratory gating.

Short- and long-axis images of the LV were acquired using the Cine Brightblood IG FLASH protocol. Sixteen cine time frames were collected to ensure the acquisition of an entire cardiac cycle. Stacks of 2D slices resulted in a resolution of 0.26 mm by 0.26 mm by 1 mm. Fast anatomies of the aorta were collected using the Planning protocol with TE/TR = 3/45 ms, 18 averages, and a flip angle of 35° to minimize imaging time, providing a spatial resolution of 0.156 mm by 0.156 mm by 0.7 mm.

### MRI data processing

Analysis of the phase-contrast MRI data involved vessel segmentation, noise masking, velocity anti-aliasing, and spatial interpolation (MATLAB 2020a). Masking was executed by using the raw data magnitude within the region where the ascending arterial structure and the actuator were apparent on the imaging plane. Velocity vectors were then calculated from the VENC (16 bit), using the phase data ($d_{\mathrm{mag}}$), denoting the velocity through the slice-plane direction, per Eq. 11

$$v_{\mathrm{mag}} = \left(\frac{d_{\mathrm{mag}}}{65,536}\right)\mathrm{VENC} \tag{11}$$

The mask was superimposed to the phase data onto the segmented borders, and aliasing correction was achieved by the unwrapping of phase data and the detection of temporal jumps greater than $\pm\pi$ at a local level. The velocity magnitude data were converted into the point cloud using the Visualization Tool Kit (VTK) libraries (VTK, Kitware Inc., NY), and the point cloud was imported into a 3D flow visualization software application (ParaView 5.9., Kitware Inc., Los Alamos National Labs).

OsiriX MD (v.13.0.1, Switzerland) was used to measure changes in aortic cross section and LV wall thickness and volume weekly for 5 weeks. The aortic cross section was computed as the cross-sectional aortic area on the slice of maximal actuator inflation. LV wall thicknesses were measured in the short-axis LV midsection during end diastole. The interventricular septum and free wall were identified by drawing a line bisecting both ventricles, and a line perpendicular to this was then drawn for posterior wall thickness calculation. LVVs were obtained by measuring the LV area (LVA) in the short-axis view, excluding papillary muscles from the LV wall, and the LV length (LVL) in the long-axis view during peak systole and end diastole per the hemisphere-cylinder model (Eq. 12) (*46*). Statistical

significance was determined using two-tailed $t$ tests with a 95% confidence interval ($P < 0.05$) on MATLAB R2020a. Statistical analysis on end-systolic volume and LV ejection fraction was conducted within each group longitudinally between the start and the end of the study

$$\mathrm{LVV} = \frac{5}{6}A \times \mathrm{LVL} \tag{12}$$

### Ultrasound evaluation

Transthoracic ultrasound evaluation of aortic flow and LV anatomy was conducted on a rat-handling platform (FUJIFILM Sonosite, Toronto, Canada) using a Vevo 3100 imaging system (FUJIFILM Sonosite, Toronto, Canada). This was equipped with an MX 201 linear array transducer (FUJIFILM Sonosite, Toronto, Canada) that was attached to a stereotactic mounting system. Two to 4% isoflurane was provided to keep the animals under general anesthesia, and the THM1500 Physiological Monitoring Unit was used to track the animal's EKG and respiratory signals during the study.

B-mode and M-mode images of the LV in parasternal long-axis and short-axis views were acquired for analysis. B-mode short-axis images were used to quantify LVA, the interventricular septum, and posterior wall and free wall thickness, whereas long-axis images were obtained to measure LVL. Pulse-wave and color Doppler imaging was performed to measure the peak flow velocity ($v_{max}$) and visualize flow. The position of the probe had to be adjusted to account for variations in the anatomy due to the surgical procedure and the presence of any scar tissue that would compromise the quality of the images. As a result, the correction angle of the pulse-wave Doppler sometimes exceeded 45°. All images were processed using the Vevo Lab 5.6 software (FUJIFILM Visualsonics, Canada).

### Histology

All animals were euthanized 2 to 3 days after final MRI evaluation using a $CO_2$ euthanasia chamber and aortic transection. The weights of the heart, lungs, and kidneys and the tibial lengths were measured using a microbalance and a caliper, respectively. The aortic and LV tissues were preserved in formalin for histological analysis. Slices were cut at a 400-μm gap. Analysis of the aortic tissue was conducted to assess the inflammatory response to the implanted actuator using H&E staining. The midsection of the LV was preserved to quantify changes in cardiomyocyte area and the degree of interstitial and perivascular fibrosis using H&E and picrosirius red stains. Tissue sectioning and staining were performed by the Histology Core of the Koch Institute for Integrative Cancer Research and the Massachusetts Institute of Technology. For all the histology data, statistical significance was determined with respect to control using two-tailed $t$ tests with a 95% confidence interval ($P < 0.05$) on MATLAB R2020a. The researchers assessing histological outcomes were blinded to the animal groups.

### Cardiomyocyte size analysis

For calculation of the volume-weighted mean volume ($Vv$) of myocardial cardiomyocytes, 10 nonoverlapping 20× H&E images were taken per sample in the myocardium. Two stereological grids (horizontal lines and crosses) were superimposed onto the images (7500 μm$^2$) using ImageJ while ensuring that the scale was previously calibrated consistently for all images. The grid size was determined by taking an average length squared of the cardiomyocytes over approximately 30 images. Using point sampled intercepts, widths of any cardiomyocyte that intersected with the cross were measured along the horizontal line. The $V_v$ of cardiomyocytes in the myocardium was therefore estimated per Eq. 13 (*47*)

$$V_V = \left(\frac{\pi}{3}\right)\mathrm{width}^3 \tag{13}$$

Twenty 20× images of the subendocardium were taken from H&E-stained sections to compute the cardiomyocyte width in the subendocardium. Images were analyzed using the CmyoSize plugin on ImageJ. This fully automated plugin standardizes cardiomyocyte size by filtering for cells that are regular and round in shape and that contain a central round nucleus and visible border (*47*, *48*).

### Interstitial and perivascular fibrosis evaluation

Systematic random sampling and point counting were used to estimate volume fraction ($V_f$) of interstitial fibrotic tissue to total interstitial space. Ten 20× images were taken in the myo- and subendocardium in picrosirius red–stained sections. A random-offset grid (2500 μm$^2$) was superimposed onto the images. Interstitial fibrosis was estimated using Eq. 14 (*49*, *50*)

$$V_f = \frac{\text{Points (fibrotic tissue)}}{\text{Points (interstitial space)} - \text{Points (fibrotic blood vessels)}} \tag{14}$$

A second count was performed on the same images to estimate the perivascular fibrosis using Eq. 15 (*49*, *50*)

$$V_f = \frac{\text{Points (fibrotic blood vessels)}}{\text{Points (interstitial space)}} \tag{15}$$

## Supplementary Materials

**This PDF file includes:**

Figs. S1 to S5
Table S1

**Other Supplementary Material for this manuscript includes the following:**

MDAR Reproducibility Checklist

## REFERENCES AND NOTES


1. P. A. Heidenreich, B. Bozkurt, D. Aguilar, L. A. Allen, J. J. Byun, M. M. Colvin, A. Deswal, M. H. Drazner, S. M. Dunlay, L. R. Evers, J. C. Fang, S. E. Fedson, G. C. Fonarow, S. S. Hayek, A. F. Hernandez, P. Khazanie, M. M. Kittleson, C. S. Lee, M. S. Link, C. A. Milano, L. C. Nnacheta, A. T. Sandhu, L. W. Stevenson, O. Vardeny, A. R. Vest, C. W. Yancy, 2022 AHA/ACC/HFSA guideline for the management of heart failure: A report of the american college of cardiology/american heart association joint committee on clinical practice guidelines. *Circulation* **145**, e895–e1032 (2022).
2. B. A. Borlaug, Evaluation and management of heart failure with preserved ejection fraction. *Nat. Rev. Cardiol.* **17**, 559–573 (2020).
3. W. J. Paulus, C. Tschöpe, A novel paradigm for heart failure with preserved ejection fraction: Comorbidities drive myocardial dysfunction and remodeling through coronary microvascular endothelial inflammation. *J. Am. Coll. Cardiol.* **62**, 263–271 (2013).
4. M. C. Tam, R. Lee, T. M. Cascino, M. C. Konerman, S. L. Hummel, Current perspectives on systemic hypertension in heart failure with preserved ejection fraction. *Curr. Hypertens. Rep.* **19**, 12 (2017).
5. B. A. Borlaug, The pathophysiology of heart failure with preserved ejection fraction. *Nat. Rev. Cardiol.* **11**, 507–515 (2014).
6. C. S. P. Lam, E. Donal, E. Kraigher-Krainer, R. S. Vasan, Epidemiology and clinical course of heart failure with preserved ejection fraction. *Eur. J. Heart Fail.* **13**, 18–28 (2011).

7. L. Rosalia, C. Ozturk, S. Shoar, Y. Fan, G. Malone, F. H. Cheema, C. Conway, R. A. Byrne, G. P. Duffy, A. Malone, E. T. Roche, A. Hameed, Device-based solutions to improve cardiac physiology and hemodynamics in heart failure with preserved ejection fraction. *JACC Basic Transl. Sci.* **6**, 772–795 (2021).
8. A. Rosenzweig, The growing importance of basic models of cardiovascular disease. *Circ. Res.* **130**, 1743–1746 (2022).
9. S. Sasayama, J. Ross Jr., D. Franklin, C. M. Bloor, S. Bishop, R. B. Dilley, Adaptations of the left ventricle to chronic pressure overload. *Circ. Res.* **38**, 172–178 (1976).
10. P. S. Douglas, S. E. Katz, E. O. Weinberg, M. H. Chen, S. P. Bishop, B. H. Lorell, Hypertrophic remodeling: Gender differences in the early response to left ventricular pressure overload. *J. Am. Coll. Cardiol.* **32**, 1118–1125 (1998).
11. A. M. Nicks, S. H. Kesteven, M. Li, J. Wu, A. Y. Chan, N. Naqvi, A. Husain, M. P. Feneley, N. J. Smith, S. E. Iismaa, R. M. Graham, Pressure overload by suprarenal aortic constriction in mice leads to left ventricular hypertrophy without c-Kit expression in cardiomyocytes. *Sci. Rep.* **10**, 15318 (2020).
12. A. K. Gs, B. Raj, K. S. Santhosh, G. Sanjay, C. Kartha, Ascending aortic constriction in rats for creation of pressure overload cardiac hypertrophy model. *J. Vis. Exp.* **88**, e50983 (2014).
13. A. C. deAlmeida, R. J. van Oort, X. H. Wehrens, Transverse aortic constriction in mice. *J. Vis. Exp.* **38**, 1729 (2010).
14. M. Valero-Muñoz, W. Backman, F. Sam, Murine models of heart failure with preserved ejection fraction: A "fishing expedition". *JACC Basic Transl. Sci.* **2**, 770–789 (2017).
15. A. C. Gomes, I. Falcão-Pires, A. L. Pires, C. Brás-Silva, A. F. Leite-Moreira, Rodent models of heart failure: An updated review. *Heart Fail. Rev.* **18**, 219–249 (2013).
16. T. Furihata, S. Kinugawa, S. Takada, A. Fukushima, M. Takahashi, T. Homma, Y. Masaki, M. Tsuda, J. Matsumoto, W. Mizushima, S. Matsushima, T. Yokota, H. Tsutsui, The experimental model of transition from compensated cardiac hypertrophy to failure created by transverse aortic constriction in mice. *Int. J. Cardiol. Heart Vasc.* **11**, 24–28 (2016).
17. A. Patel, D. Patel, Congestive heart failure model representing aortic banding induced hypertrophy: A study to analyse extent of pressure overload and alteration in myocardial structure and function. *Int. J. Cardiol. Heart Vasc.* **34**, 100755 (2021).
18. D. A. Richards, M. J. Aronovitz, T. D. Calamaras, K. Tam, G. L. Martin, P. Liu, H. K. Bowditch, P. Zhang, G. S. Huggins, R. M. Blanton, Distinct phenotypes induced by three degrees of transverse aortic constriction in mice. *Sci. Rep.* **9**, 5844 (2019).
19. X. Zhang, H. Javan, L. Li, A. Szucsik, R. Zhang, Y. Deng, C. H. Selzman, A modified murine model for the study of reverse cardiac remodelling. *Exp. Clin. Cardiol.* **18**, e115–e117 (2013).
20. A. O. Melleby, A. Romaine, J. M. Aronsen, I. Veras, L. Zhang, I. Sjaastad, I. G. Lunde, G. Christensen, A novel method for high precision aortic constriction that allows for generation of specific cardiac phenotypes in mice. *Cardiovasc. Res.* **114**, 1680–1690 (2018).
21. D. Merino, A. Gil, J. Gómez, L. Ruiz, M. Llano, R. García, M. A. Hurlé, J. F. Nistal, Experimental modelling of cardiac pressure overload hypertrophy: Modified technique for precise, reproducible, safe and easy aortic arch banding-debanding in mice. *Sci. Rep.* **8**, 3167 (2018).
22. C. Perrino, S. V. Naga Prasad, L. Mao, T. Noma, Z. Yan, H. S. Kim, O. Smithies, H. A. Rockman, Intermittent pressure overload triggers hypertrophy-independent cardiac dysfunction and vascular rarefaction. *J. Clin. Invest.* **116**, 1547–1560 (2006).
23. R. Hinkel, S. Batkai, A. Bähr, T. Bozoglu, S. Straub, T. Borchert, J. Viereck, A. Howe, N. Hornaschewitz, L. Oberberger, V. Jurisch, R. Kozlik-Feldmann, F. Freudenthal, T. Ziegler, C. Weber, M. Sperandio, S. Engelhardt, K. L. Laugwitz, A. Moretti, N. Klymiuk, T. Thum, C. Kupatt, AntimiR-132 attenuates myocardial hypertrophy in an animal model of percutaneous aortic constriction. *J. Am. Coll. Cardiol.* **77**, 2923–2935 (2021).
24. D. Xu, N. Li, Y. He, V. Timofeyev, L. Lu, H. J. Tsai, I. H. Kim, D. Tuteja, R. K. P. Mateo, A. Singapuri, B. B. Davis, R. Low, B. D. Hammock, N. Chiamvimonvat, Prevention and reversal of cardiac hypertrophy by soluble epoxide hydrolase inhibitors. *Proc. Natl. Acad. Sci. U.S.A.* **103**, 18733–18738 (2006).
25. W. E. Stansfield, P. C. Charles, R. H. Tang, M. Rojas, R. Bhati, N. C. Moss, C. Patterson, C. H. Selzman, Regression of pressure-induced left ventricular hypertrophy is characterized by a distinct gene expression profile. *J. Thorac. Cardiovasc. Surg.* **137**, 232–238.e8 (2009).
26. X. M. Gao, H. Kiriazis, X. L. Moore, X. H. Feng, K. Sheppard, A. Dart, X. J. du, Regression of pressure overload-induced left ventricular hypertrophy in mice. *Am. J. Physiol. Heart Circ. Physiol.* **288**, H2702–H2707 (2005).
27. W. E. Stansfield, M. Rojas, D. Corn, M. Willis, C. Patterson, S. S. Smyth, C. H. Selzman, Characterization of a model to independently study regression of ventricular hypertrophy. *J. Surg. Res.* **142**, 387–393 (2007).
28. L. Rosalia, C. Ozturk, D. Goswami, J. Bonnemain, S. X. Wang, B. Bonner, J. C. Weaver, R. Puri, S. Kapadia, C. T. Nguyen, E. T. Roche, Soft robotic patient-specific hydrodynamic model of aortic stenosis and ventricular remodeling. *Sci. Rob.* **8**, eade2184 (2023).
29. L. Rosalia, C. Ozturk, J. Coll-Font, Y. Fan, Y. Nagata, M. Singh, D. Goswami, A. Mauskapf, S. Chen, R. A. Eder, E. M. Goffer, J. H. Kim, S. Yurista, B. P. Bonner, A. N. Foster, R. A. Levine, E. R. Edelman, M. Panagia, J. L. Guerrero, E. T. Roche, C. T. Nguyen, A soft robotic sleeve mimicking the haemodynamics and biomechanics of left ventricular pressure overload and aortic stenosis. *Nat. Biomed. Eng.* **6**, 1134–1147 (2022).
30. L. Rosalia, C. Ozturk, S. X. Wang, D. Quevedo-Moreno, M. Y. Saeed, A. Mauskapf, E. T. Roche, Modulating cardiac hemodynamics using tunable soft robotic sleeves in a porcine model of HFpEF physiology for device testing applications. *Adv. Funct. Mater.* **34**, 2310085 (2023).
31. M. Saeed, T. A. Van, R. Krug, S. W. Hetts, M. W. Wilson, Cardiac MR imaging: Current status and future direction. *Cardiovasc. Diagn. Ther.* **5**, 290–310 (2015).
32. T. A. Roberts, A. N. Price, L. H. Jackson, V. Taylor, A. L. David, M. F. Lythgoe, D. J. Stuckey, Direct comparison of high-temporal-resolution CINE MRI with Doppler ultrasound for assessment of diastolic dysfunction in mice. *NMR Biomed.* **30**, e3763 (2017).
33. J. S. Cho, E. J. Cho, J. Lee, H. D. Choi, K. C. Park, K. H. Lee, K. J. Yang, M. W. Park, G. M. Park, S. H. Her, C. J. Kim, Myocardial mechanics in a rat model with banding and debanding of the ascending aorta. *J. Cardiovasc. Ultrasound.* **22**, 189–195 (2014).
34. T. Chen, F. Shao, K. Chen, Y. Wang, Z. Wu, Y. Wang, Y. Gao, V. Cornelius, C. Li, Z. Jiang, Time to clinical benefit of intensive blood pressure lowering in patients 60 years and older with hypertension: A secondary analysis of randomized clinical trials. *JAMA Intern. Med.* **182**, 660–667 (2022).
35. T. Sevilla, A. Revilla-Orodea, J. A. San Román, Timing of intervention in asymptomatic patients with aortic stenosis. *Eur. Cardiol.* **16**, e32 (2021).
36. R. J. Everett, M. A. Clavel, P. Pibarot, M. R. Dweck, Timing of intervention in aortic stenosis: A review of current and future strategies. *Heart* **104**, 2067–2076 (2018).
37. A. N. Smith, R. Altara, G. Amin, N. J. Habeichi, D. G. Thomas, S. Jun, A. Kaplan, G. W. Booz, F. A. Zouein, Genomic, proteomic, and metabolic comparisons of small animal models of heart failure with preserved ejection fraction: A tale of mice, rats, and cats. *J. Am. Heart Assoc.* **11**, e026071 (2022).
38. J. Roh, J. A. Hill, A. Singh, M. Valero-Muñoz, F. Sam, Heart failure with preserved ejection fraction: Heterogeneous syndrome, diverse preclinical models. *Circ. Res.* **130**, 1906–1925 (2022).
39. G. Conceição, I. Heinonen, A. P. Lourenço, D. J. Duncker, I. Falcão-Pires, Animal models of heart failure with preserved ejection fraction. *Neth. Heart J.* **24**, 275–286 (2016).
40. Y. Yao, S. Chen, Z. Huang, A generalized Ogden model for the compressibility of rubber-like solids. *Philos. Trans. R. Soc. A* **380**, 20210320 (2022).
41. N. Saikrishnan, G. Kumar, F. J. Sawaya, S. Lerakis, A. P. Yoganathan, Accurate assessment of aortic stenosis. *Circulation* **129**, 244–253 (2014).
42. H. Baumgartner, J. Hung, J. Bermejo, J. B. Chambers, T. Edvardsen, S. Goldstein, P. Lancellotti, M. L. Fevre, F. Miller Jr., Recommendations on the echocardiographic assessment of aortic valve stenosis: A focused update from the European Association of Cardiovascular Imaging and the American Society of Echocardiography. *Eur. Heart J. Cardiovasc. Imaging* **18**, 254–275 (2017).
43. P. Pibarot, D. Messika-Zeitoun, O. Ben-Yehuda, R. T. Hahn, I. G. Burwash, N. van Mieghem, E. Spitzer, M. B. Leon, J. Bax, C. M. Otto, Moderate aortic stenosis and heart failure with reduced ejection fraction: Can imaging guide us to therapy? *JACC Cardiovasc. Imaging* **12**, 172–184 (2019).
44. R.-J. Nuis, J. A. Goudzwaard, M. J. A. G. de Ronde-Tillmans, H. Kroon, J. F. Ooms, M. P. van Wiechen, M. L. Geleijnse, F. Zijlstra, J. Daemen, N. M. van Mieghem, F. U. S. Mattace-Raso, M. J. Lenzen, P. P. T. de Jaegere, Impact of valvulo-arterial impedance on long-term quality of life and exercise performance after transcatheter aortic valve replacement. *Circ. Cardiovasc. Interv.* **13**, e008372 (2020).
45. M. Farriol, J. Rosselló, S. Schwartz, Body surface area in Sprague-Dawley rats. *J. Anim. Physiol. Anim. Nutr.* **77**, 61–65 (1997).
46. T. Arias, J. Chen, Z. A. Fayad, V. Fuster, R. J. Hajjar, E. R. Chemaly, Comparison of echocardiographic measurements of left ventricular volumes to full volume magnetic resonance imaging in normal and diseased rats. *J. Am. Soc. Echocardiogr.* **26**, 910–918 (2013).
47. R. E. Tracy, G. E. Sander, Histologically measured cardiomyocyte hypertrophy correlates with body height as strongly as with body mass index. *Cardiol. Res. Pract.* **2011**, 658958 (2011).
48. F. S. da Silva, N. C. S. Aquino de Souza, M. V. de Moraes, B. J. Abreu, M. F. de Oliveira, CmyoSize: An ImageJ macro for automated analysis of cardiomyocyte size in images of routine histology staining. *Ann. Anat.* **241**, 151892 (2022).
49. H. J. Gundersen, P. Bagger, T. F. Bendtsen, S. M. Evans, L. Korbo, N. Marcussen, A. MØLLer, K. Nielsen, J. R. Nyengaard, B. Pakkenberg, F. B. SØRensen, A. Vesterby, M. J. West, The new stereological tools: Disector, fractionator, nucleator and point sampled intercepts and their use in pathological research and diagnosis. *APMIS* **96**, 857–881 (1988).
50. J. Schipke, C. Brandenberger, A. Rajces, M. Manninger, A. Alogna, H. Post, C. Mühlfeld, Assessment of cardiac fibrosis: A morphometric method comparison for collagen quantification. *J. Appl. Physiol.* **122**, 1019–1030 (2017).

**Acknowledgments:** We thank the Koch Institute's Robert A. Swanson (1969) Biotechnology Center for technical support, specifically the histology, the preclinical modeling, and the preclinical imaging and testing facilities. We acknowledge E. Franklin and the Department of Comparative Medicine at Massachusetts Institute of Technology for support during the animal studies and R. Bronson and the Rodent Pathology Core at Harvard Medical School for assistance with the histopathology studies. **Funding:** This work was supported by the National Science Foundation, 1847541 (E.T.R.); NIH training grant T32 HL007734 (S.X.W.); the Lausanne University Improvement fund (J.B.); and the Koch Institute Support Grant P30-CA14051 from the National Cancer Institute.
**Author contributions:** L.R., S.X.W., and E.T.R. designed the study. L.R. and S.X.W. performed all experiments and wrote the paper. C.O., W.H., and J.B. provided experimental support. R.B., G.P.D., and C.N.T. provided analysis support. E.T.R. provided funding. **Competing interests:** E.T.R. is on the board of directors for Affluent Medical and Helios Cardio and the board of scientific advisors for Pumpinheart, consults for Holistick Medical, and is an academic cofounder of Fada Medical and Spheric Bio. G.P.D. is an academic cofounder of Fada Medical and FeelTect Limited. The authors declare that they have no competing interests. **Data and materials availability:** All data needed to support the conclusions of this manuscript are included in the main text or Supplementary Materials. Data analysis code is publicly available at 10.5281/zenodo.10015294.

Submitted 26 July 2023
Accepted 17 May 2024
Published 12 June 2024
10.1126/scirobotics.adj9769

Science Robotics

# Soft robotic platform for progressive and reversible aortic constriction in a small-animal model

Luca Rosalia, Sophie X. Wang, Caglar Ozturk, Wei Huang, Jean Bonnemain, Rachel Beatty, Garry P. Duffy, Christopher T. Nguyen, and Ellen T. Roche

*Sci. Robot.* **9** (91), eadj9769. DOI: 10.1126/scirobotics.adj9769

**Editor's summary**

Understanding the processes involved in heart failure due to cardiac diseases is crucial in the development of effective interventions. However, tunable physical models that can suitably replicate these processes progressively are lacking. Rosalia *et al.* have now used implantable soft robot actuators to develop a tunable platform that can model progressive and reversible aortic constriction in small animals. With the aid of magnetic resonance imaging, they demonstrated the hemodynamic changes due to pressure overload from aortic banding and debanding, replicating the progression and reversal of cardiac disease. —Amos Matsiko